Int J Appl Earth Obs Geoinformation 89 (2020) 102088

Contents lists available at ScienceDirect

Int J Appl Earth Obs Geoinformation

journal homepage: www.elsevier.com/locate/jag

Sensitivity and uncertainty quantification for the ECOSTRESS evapotranspiration algorithm – DisALEXI

Kerry Cawse-Nicholson[a,*], Amy Braverman[a], Emily L. Kang[b], Miaoqi Li[b], Margaret Johnson[a], Gregory Halverson[a], Martha Anderson[c], Christopher Hain[d], Michael Gunson[a], Simon Hook[a]

[a] Jet Propulsion Laboratory, California Institute of Technology, United States
[b] University of Cincinnati, OH, United States
[c] United States Department of Agriculture, United States
[d] NASA Marshall Space Flight Center, United States

ARTICLE INFO

Keywords:
Uncertainty
Spatial statistics
disALEXI
Evapotranspiration

ABSTRACT

Evapotranspiration (ET) is a measure of plant water use that is utilized regionally for drought detection and monitoring, and locally for agricultural water resource management. Understanding the uncertainty associated with this measurement is vital for science predictions and analysis and for water resource management decision making. In this manuscript, the uncertainty in disaggregated Atmosphere-Land Exchange (disALEXI) is quantified; disALEXI is an ET algorithm that utilizes land surface temperature (LST) derived from the ECOsystem Spaceborne Thermal Radiometer Experiment on Space Station (ECOSTRESS), as well ancillary inputs for land-cover, elevation, vegetation parameters, and meteorological inputs. Since each of these inputs has an associated, and potentially unknown, uncertainty, in this study a Monte Carlo simulation based on a spatial statistical model is used to determine the algorithm's sensitivity to each of its inputs, and to quantify the probability distribution of algorithm outputs. Analysis shows that algorithm is most sensitive to LST (the input derived from ECOSTRESS). Significantly, the output uncertainty distribution is non-Gaussian, due to the non-linear nature of the algorithm. This means that ET uncertainty cannot be prescribed by accuracy and precision alone. Here, uncertainty was represented using five quantiles of the output distribution. The distribution was consistent across five different datasets (mean offset is 0.01 mm/day, and 95% of the data is contained within 0.3 mm/day). An additional two datasets with low ET, showed higher uncertainty (95% of the data is within 1 mm/day), and a positive bias (i.e., ET was overestimated by an average of 0.12 mm/day when ET was low).

1. Introduction

The ECOsystem Spaceborne Thermal Radiometer Experiment on Space Station (ECOSTRESS) was launched on June 29th, 2018, and measures the earth's surface temperature in order to detect vegetation stress. ECOSTRESS is a fine-resolution (70 m), multiple-wavelength, imaging radiometer that captures light in the thermal part of the electromagnetic spectrum. It takes measurements in three spectral bands between 8 and 12.5 μm. ECOSTRESS was designed to address the response of the terrestrial biosphere to changes in water availability, the impact of diurnal vegetation water stress on the global carbon cycle, and reduction in agricultural vulnerability through improved water resource management.

In order to achieve these goals, ECOSTRESS is used to determine evapotranspiration (ET), a combination of plant surface evaporation of water (from soils and water intercepted by plant canopies), and the transpiration from plant leaves and stems (released via the stomata). The stomatal behavior is driven by light levels, soil water availability, temperature and vapor pressure, and the stomata will close if the plant is water-stressed (Mu et al., 2011). Therefore, a reduction in ET is an indicator for vegetation stress, and this change happens before the vegetation loses greenness (Anderson et al., 2016).

After precipitation, ET is the largest global contributor to the terrestrial water cycle, returning up to 60% of precipitated water to the atmosphere (Mu et al., 2011). Therefore, accurate estimation of ET with fully characterized uncertainties is vital in order to understand the hydrological cycle. Accurate ET monitoring at the scale of an agricultural field will provide the tools to identify small areas where changes in land and water management will have the greatest effect on food security (Anderson et al., 2016). Uncertainty is defined as the

* Corresponding author.
E-mail address: kcawseni@jpl.nasa.gov (K. Cawse-Nicholson).

https://doi.org/10.1016/j.jag.2020.102088
Received 31 October 2019; Received in revised form 11 February 2020; Accepted 11 February 2020
0303-2434/ © 2020 The Authors. Published by Elsevier B.V. This is an open access article under the CC BY-NC-ND license (http://creativecommons.org/licenses/BY-NC-ND/4.0/).

probability distribution of the model output about true ET. Information about this distribution is required for making inferences in subsequent applications of the ET product. For example, water resource managers rely on knowledge of the ET and uncertainty in order to make informed decisions, and drought forecast models require uncertainty in order to propagate those values through their own models to determine forecast accuracies.

Generally, there are three classes of techniques that are used to calculate ET from remotely sensed data: empirical models that relate ET to certain vegetation indices; physical models that calculate ET directly; and physical models that calculate ET as the residual of the surface energy balance, such as the Atmosphere Land Exchange model (ALEXI) and the disaggregated form of the algorithm, disALEXI. This manuscript proposes a methodology that provides a way to characterize and then propagate input uncertainties through the disALEXI ET model. This is a framework that enables both sensitivity analysis and uncertainty quantification, where the input uncertainty is modeled using a multivariate spatial-statistical model. This framework is demonstrated in several real ECOSTRESS examples. In addition, this work aims to investigate whether the final uncertainty can be adequately described by traditional metrics such as accuracy and precision (which assume that the uncertainty is Gaussian).

In this manuscript, uncertainty in disALEXI ET estimates is quantified using a Monte Carlo approach to propagate uncertainties through the disALEXI algorithm. Section 3 describes the disALEXI model that is used to generate estimates of ET from ECOSTRESS data. Since true ET is unknown, uncertainty is quantified through a simulation experiment that generates an ensemble of synthetic, true spatial fields derived from an ECOSTRESS parent input field. The underlying assumption is that the relationship between the synthetic ensemble members and the parent data is similar to the relationship between the parent data field itself and the true ET field. To simulate the ensemble members, a spatial-statistical model was fitted to the parent data, and then the ensemble members were simulated from that model. The model preserves realistic spatial and inter-variable correlation structures; details are given in Section 4. Results are provided in Section 6. Finally, there is a discussion of significance, and means by which to provide this uncertainty information to the user community.

2. Background

Currently, several ET products are available, and each has its own definition of uncertainty. Mapping ET with high Resolution and Internalized Calibration (METRIC) uses Landsat imagery and is applied to scenes with associated in-scene information and weather stations (Allen et al., 2007). METRIC has been applied to sites in several states in the US. The algorithm requires site-specific calibration, and the sensitivity of this calibration has been studied in Morton et al. (2013). In that study, 100 Monte Carlo runs were used to randomly select pixel samples from the input Landsat imagery, which were used to set the calibration coefficients, and the overall sensitivity was presented as a mean, standard deviation, and coefficient of variation (Morton et al., 2013). The average "uncertainty" was defined by the sensitivity analysis and was determined to be 5% of the true value.

Other models, such as the Surface Energy Balance Algorithm over Land (SEBAL) (Bastiaanssen et al., 1998) and Surface Energy Balance System (SEBS) (Su, 2002) combine satellite remote sensing with ancillary inputs to estimate the residual of the surface energy balance model. Analysis for SEBAL showed that the ET outputs were non-Gaussian, and therefore, the authors in Kiptala et al. (2013) used non-parametric statistical inference methods to test the difference between SEBAL and the MODIS global ET product — MOD16. This was defined as the "uncertainty quantification" for the study done by Kiptala et al. (2013). A Bayesian Inference study was carried out in order to study the "uncertainty" in SEBS for twelve flux towers (Ershadi et al., 2013). The mean and standard deviation of inputs measured by the flux tower was used as the prior, and the simulated ET was compared to measured ET in order to determine sensitivity. The algorithm was most sensitive to LST.

MOD16 1 km ET products are available for the time period 2000–2014, with regular, but not real-time, updates to the temporal extent. MOD16 accepts albedo and meteorological input, using an algorithm based on modifications to the Penman–Monteith equation (Mu et al., 2011). This product is distributed without an associated uncertainty, and an evaluation of MOD16 "uncertainty" described in Khan et al. (2018) is a comparison with field data. Another study showed a comparison between land surface models and diagnostic ET datasets, and produced "uncertainty" as the standard deviation of the differences across grid cells in the image, as well as analyzing sensitivities to different inputs such as meteorological forcings, and landcover class (Jung et al., 2019).

The Priestley–Taylor (PT) model is also widely used, and a modified version, PT-JPL, has historically been applied globally using AVHRR and ISLSCP-II data (Fisher et al., 2008). The data product is available for the time period 1986–1995 at 0.5° resolution and 1986–2006 at 1° resolution.[1] PT-JPL is the second ET algorithm used for ECOSTRESS, and an "uncertainty" field is provided as the standard deviation over the application of several different methods, including Priestley-Taylor, Penman–Monteith, and TSEB (Fisher, 2018). One study compared the uncertainty of global, monthly ET generated by PT-JPL, by comparing a set of different sources for each input (Badgley et al., 2015). Net radiation was determined to be the largest contributor based on differences in ET dependent on different net radiation input sources. A sensitivity study carried out in Fisher et al. (2013) showed that an input LST with uncertainty ≤1 K would result in an ET accuracy ≤10% (Fisher et al., 2017).

In the United States, the National Oceanic and Atmospheric Administration (NOAA) uses ET to produce an Evaporative Stress Index (ESI), which represents standardized anomalies in the ratio of actual ET to potential ET (thereby normalizing out atmospheric drivers on ET, and focusing on surface moisture constraints) as a metric for drought monitoring. This product is available over the continental US, and uses Geostationary Operational Environmental Satellites (GOES; 4 km spatial resolution) as input to the Atmosphere Land-Exchange (ALEXI) model (Anderson et al., 1997) – a surface energy balance algorithm driven primarily by thermal infrared retrievals of land-surface temperature. The ESI product is produced without associated uncertainty.

There is significant variation in the definition of "uncertainty" in this community. Uncertainty quantification has been defined as a sensitivity analysis (Morton et al., 2013), as a model comparison (PT-JPL) (Kiptala et al., 2013), and as a validation against field data (Khan et al., 2018). In this manuscript, uncertainty quantification is understood to be *none of the above*, and is defined purely as model output uncertainty that results from reasonable perturbations of the inputs.

3. ET model

The ET spatial field is derived through a two-step procedure. First the Atmosphere Land-Exchange Inverse (ALEXI) model (Anderson et al., 1997) ingests a set of inputs (see Table 1) and outputs ET estimates at 4 km spatial resolution. Then, ET is downscaled through a disaggregation algorithm called disALEXI. For the Jet Propulsion Laboratory implementation of disALEXI, ET is downscaled to 70 m ECOSTRESS resolution (other implementations rescale to 30 m Landsat visible band resolution). This section contains a brief overview of the ALEXI model, the disALEXI algorithm, and the input data required to run them.

[1] www.landflux.org/Data.php.

Table 1
Input data required for disALEXI processing. *i* is variable index, and *j* indexes variable sets. Variables in the same set will be treated jointly. Cont. and Cat. in column 3 denote continuous and categorical respectively. All datasets are publicly available, with the exception of ALEXI ET, which is hosted at Marshall Space Flight Center. The original resolution of the input data is shown here, but all data are spatially and temporally interpolated to ECOSTRESS resolution before being used in this manuscript.

i	*j*	Variable	Type	Dataset	Source	Spat res.	Temp res.
1	1	Alb	Cont.	Landsat8 (Survey, 2015)	EROS	30 m	16d
2	1	NDVI	Cont.	Landsat8 (Survey, 2015)	EROS	30 m	16d
3	1	LAI	Cont.	Landsat8/ MCD15A3H (Myneni et al., 2015)	EROS/ LP DAAC	30 m 1 km	16d/ 1d
4	1	LST	Cont.	L2_LSTE	ECOSTRESS	70 m	1-7d
5	2	Ins	Cont.	CFSR (Saha et al., 2011)	NCAR	0.5°	1h
6	2	Ins-avg insolation	Cont.	CFSR (Saha et al., 2011)	NCAR	0.5°	1d
7	3	Wind	Cont.	CFSR (Saha et al., 2011)	NCAR	0.5°	3 h
8	4	AT	Cont.	CFSR (Saha et al., 2011)	NCAR	0.5°	3 h
9	5	VZ	Cont.	L1B_GEO (Hook, 2019)	ECOSTRESS	70 m	1–7d
10	–	ALEXI ET	Cont.	MSFC	NASA	4 km	1d
11	–	Elevation	Cont.	SRTM (USGS, 2004)	EROS	30 m	–
12	–	Landcover	Cat.	NLCD (Homer et al., 2015)	MRLC	30 m	–

3.1. ALEXI

The Atmosphere Land-Exchange (ALEXI) model (Anderson et al., 1997) surface energy balance model was designed to minimize sensitivity to errors in both input land-surface temperature and air temperature boundary conditions. To accomplish this ALEXI uses time-differential measurements of the morning surface temperature rise obtained from geostationary satellite platforms as the primary remote sensing input. This time-differential approach minimizes latent heat flux errors due to absolute thermal sensor calibration and atmospheric and emissivity corrections, which can cause biases in ET estimates. Furthermore, above-canopy air temperature boundary conditions are not prescribed but rather derived internally using a coupled atmospheric boundary layer model, effectively incorporating impacts of localized land-atmosphere feedback which may be neglected in regional temperature re-analyses.

ALEXI applies the "series" version of the Two-Source Energy Balance (TSEB) model of Norman et al. (1995) at two times during the morning - about an hour after sunrise and an hour before local noon. The TSEB partitions the surface radiometric temperature and fluxes into soil (subscript 's') and canopy (subscript 'c') components, based on the local vegetation cover fraction. The latent heat flux at each time, λE, is computed as $\lambda E = \lambda E_c + \lambda E_s = R_{\text{net}} - H - G$, where R_{net} is net radiation, G is the soil heat conduction flux and H is the sensible heat flux from the surface to the atmosphere. Energy closure over the morning interval is iteratively computed between the surface and boundary layer components of the model. Finally, latent heat at time 2 is upscaled to a daily energy flux (λE_d; MJ m^{-2} d^{-1}) using insolation as the scaling flux, and converted to evapotranspiration (ET; mm d^{-1}) as $\text{ET} = \lambda E_d/(\rho^*\lambda)$ where λ is the latent heat of vaporization (MJ/g) and ρ is the density of water (kg/m^3).

3.2. disALEXI

For finer resolution assessments (e.g., at 70 m ECOSTRESS scale), a disaggregation scheme (disALEXI) has been developed to downscale the 4-km GOES-derived ALEXI ET product (Norman et al., 2003; Anderson et al., 2004). In disALEXI, the TSEB is applied to the high-resolution thermal data using a re-analysis air temperature field as an initial upper boundary condition at a nominal blending height for a second, high resolution implementation of ALEXI, which uses data from ECOSTRESS and Landsat. Latent heat at the ECOSTRESS overpass time is scaled to daily ET as in ALEXI. The air temperature boundary is then iteratively modified on the scale of an ALEXI pixel such that the average daily ET flux from disALEXI matches the coarser scale daily ALEXI flux (Anderson et al., 2012), ensuring consistency in flux distribution across scales. In this way, the algorithm utilizes the benefit of fine-resolution ET estimation, while maintaining the benefit of using a time differential to calculate the coarser-resolution ET to reduce the impact of atmospheric corrections and other error sources.

3.3. Inputs

The ECOSTRESS implementation of disALEXI takes the following inputs: albedo (Alb), normalized difference vegetation index (NDVI), leaf area index (LAI), LST, viewing zenith angle (VZ), landcover, elevation, wind speed(3 hourly; Wind), air temperature 30 m above ground (3 hourly; AT), short-wave downward solar radiation (insolation, hourly; Ins), and the coarse resolution daily ALEXI product at 4km resolution. ECOSTRESS LST retrievals used in disALEXI are constrained to occur during daylight hours, using solar zenith angle as the determinant. The albedo and vegetation parameters are determined from the nearest Landsat8 overpass; the landcover map is produced by matching to the National Landcover Database (NLCD), produced by the Multi-Resolution Land Cover Characteristics (MRLC) Consortium; the average scene elevation is calculated from the Shuttle Radar Terrain Mission (SRTM); the meteorological data are obtained from the Climate Forecast System (CFSv2) Operational Analysis; and the ALEXI ET product is calculated daily and hosted at the Short-term Prediction Research and Transition Center (SPoRT), Marshall Space Flight Center (MSFC). Prior to simulation, all data have been interpolated to ECOSTRESS resolution in both space and time using the Python package *pyresample*[2] with bilinear interpolation (Fisher, 2018). This ensures smoothness in the resampled spatial-temporal field. The inputs are detailed in Table 1. Notably, none of the input variables come with uncertainties, except for LST, provided by ECOSTRESS.

The standard ECOSTRESS LST uncertainty is simulated by constructing a wide range of feasible conditions, and using radiative transfer code to propagate these conditions through to temperature and emissivity retrieval. The uncertainty is parameterized as a function of the dominant sources of error: view angle and total column water vapor (Hulley, 2018).

Since almost all of the inputs do not come with associated uncertainties, one needs a way to characterize representative uncertainty in the input, which can be done through a statistical model. For consistency, in this manuscript, the LST uncertainty is simulated using a statistical model, in the same manner as the other inputs.

[2] https://pyresample.readthedocs.io/en/latest/.

4. Methods

One may simulate an ensemble of spatial fields of ET input variables shown in Table 1 by fitting a spatial-statistical model (Cressie, 1993) (Cressie and Wikle, 1993) to a parent spatial field, and generating realizations from that model. Let the number of realizations be B. The parent field for a particular scene is the actual data used in ECOSTRESS processing. Each ensemble member generated from model, $b = 1, \ldots, B$, inherits the spatial and inter-variable dependence structure of the parent, but differs according to internal variability. Internal variability is quantified by estimating the model's parameters from the parent data. Uncertainty in ET estimates produced by disALEXI is quantified by (1) applying the disALEXI processing chain to all pixels in all ensemble members in a Monte Carlo process, and (2) examining the distributions of the B ET values at individual pixels, and the covariances between pixels calculated from the ensembles. Appendix A provides details of the spatial-statistical modeling procedure for the interested reader.

This method simulates 100 sets of inputs, where each input maintains both spatial and between-variable correlation. Each of these 100 sets of inputs are then run through the disALEXI in Monte Carlo fashion, in order to determine the ultimate effect on uncertainty.

5. Datasets

The modeling and simulation methodology described in Section 4 was applied to seven ECOSTRESS scenes collected over the United States at single time instances during August 2018. The scenes are enumerated in Table 2, and displayed in Fig. 1, which shows the output of the disALEXI model. The selection was limited to a single month in order to eliminate the impact of seasonal changes by holding time essentially constant. A summer month was chosen because summer is the growing season in much of the US, and because conditions were cloud-free at the scenes under consideration at that time of year.

The scenes were also selected primarily because they were cloud- and artefact-free, and also in order to provide an assortment of different conditions. Six of the scenes are in California, and one is in Nebraska. Each scene is a 400 × 400 spatial array of 70-m pixels covering regions of approximately 28 km × 28 km. Scene A is an agricultural region in the Imperial Valley. Scene B is a different part of the same acquisition, and shows a discrete change from agriculture to dry, barren surroundings. Scene C is an agricultural area containing mostly irrigated and rainfed corn and soybean in Nebraska, and Scene D is an oakland savannah with medium ET values. Scene E is another agricultural area with low ET, and Scene F has a strong gradient from the agricultural area on the left, to grasslands on the right. Scene G is a forested site at high elevation, where topographic shadowing and enhanced roughness in the terrain (uncorrected for in JPL disALEXI) tend to lead to overestimation in ET, based on expert knowledge of the algorithm's developer (personal communication). This case serves as a test to see whether high ET is associated with high uncertainty. The horizontal striping in Scene F is an artifact of the ECOSTRESS observing geometry; ECOSTRESS is a push-whisk instrument, and the horizontal lines are the result of overlapping scanlines, which will be corrected during geolocation.

Table 2
Seven 400 × 400 pixel subsets (approximately 28 km × 28 km) selected for evaluation. Key differences between scenes are highlighted in italics. These include location differences, and land-use type (e.g., agriculture vs. non-agriculture).

Scene	Latitude	Longitude	Date	Time	Description
A	33.0865	−115.5246	2018-08-31	18:55	Agriculture
B	33.6657	−114.5690	2018-08-31	18:55	Agriculture
C	*42.2543*	*−103.1203*	2018-08-24	20:09	Agriculture
D	38.3917	−120.9957	2018-08-27	20:44	*Oak Savannah*
E	38.5425	−121.8688	2018-08-27	20:44	Agriculture
F	37.1464	−120.0562	2018-08-27	20:45	*Grassland*
G	38.5433	−120.5148	2018-08-28	19:52	*Forest*

The filenames of the ECOSTRESS inputs are given in Appendix B.

6. Analysis and results

Two analyses were performed using the simulation results described above: a sensitivity study and full uncertainty quantification. Both studies use a Monte Carlo simulation using as inputs the ensemble of $B = 100$ simulated spatial fields, for each scene, that were created using the methodology described above.

Denote the parent input fields for Scenes A through G by $\mathbf{X}_{A0}$ through $\mathbf{X}_{G0}$ and the corresponding parent ET fields by $\mathbf{E}_{A0}$ through $\mathbf{E}_{G0}$. Denote the bth simulated field of input vectors by $\mathbf{X}_{\mathrm{Ab}}$ through $\mathbf{X}_{\mathrm{Gb}}$, and the (scalar-valued) ET output fields by $\mathbf{E}^*_{\mathrm{Ab}}$ through $\mathbf{E}^*_{\mathrm{Gb}}$. If $b = 0$ corresponds to the parent field and $b = 1, \ldots, B = 100$ corresponds to simulated fields derived from the parent, then the nth pixel of the bth input field for Scene k is,

$$\mathbf{X}_{\mathrm{kb}}(\mathbf{s}_n) = (X_{\mathrm{kb1}}(\mathbf{s}_n), \ldots, X_{\mathrm{kbM}}(\mathbf{s}_n))',$$

where $X_{\mathrm{kbi}}(\mathbf{s}_n)$ is the value of the ith input variable (see Table 1), $i = 1, \ldots, 12$ and $k = A, B, C, D, E, F, G$.

6.1. Sensitivity analysis

The goal of sensitivity analysis is to determine which variables are most influential in the determination of ET derived by disALEXI. A set of experiments were performed for each scene in which all but one input variables were held fixed at their parent data set values. The input that was allowed to vary, called the target, assumed 100 different values generated by the simulation described in the previous section. The empirical standard deviations of ET values under these conditions are shown in Table 3 wherein each input successively played the role of the target.

The nine experiments followed the procedure below:

1. Set the target variable, $i = 1$.
2. For $n = 1, \ldots, N$ and $b = 1, \ldots, B = 100$ set

$$X^*_{\mathrm{kbm}}(\mathbf{s}_n, i) = \begin{cases} X_{k0m}(\mathbf{s}_n) & \text{if } m \neq i, \\ X_{\mathrm{kbm}}(\mathbf{s}_n) & \text{if } m = i, \end{cases} \quad m = 1, \ldots, 9.$$

   Recall that, of the twelve inputs, ALEXI ET ($m = 10$) and elevation ($m = 11$), and landcover ($m = 12$) are fixed, and never assume the role of target variable.
3. Set

$$\mathbf{X}^*_{\mathrm{kb}}(\mathbf{s}_n, i) = (X^*_{\mathrm{kb1}}(\mathbf{s}_n, i), \ldots, X^*_{\mathrm{kbM}}(\mathbf{s}_n, i))',$$
$$\mathbf{X}^*_{\mathrm{kb}}(i) = (\mathbf{X}^*_{\mathrm{kb}}(\mathbf{s}_1, i), \ldots, \mathbf{X}^*_{\mathrm{kb}}(\mathbf{s}_n, i))'.$$

   The bth simulated spatial field for Scene k and target variable i is $\mathbf{X}^*_{\mathrm{kb}}(i)$.
4. For $b = 1, \ldots, B = 100$, apply the disALEXI algorithm to $\mathbf{X}^*_{\mathrm{kb}}(i)$ to obtain $\mathbf{E}^*_{\mathrm{kb}}(i)$, the bth simulated ET spatial field for target variable i,

$$\mathbf{E}^*_{\mathrm{kb}}(i) = (E^*_{\mathrm{kb}}(\mathbf{s}_1, i), \ldots, E^*_{\mathrm{kb}}(\mathbf{s}_N, i))'.$$

5. Set i to $i + 1$ and repeat until $i > 10$.

Table 3 shows the empirical standard deviations of ET, $\sigma^{\mathrm{s}}_{\mathrm{ET}}(i)$, over all N pixels and $B = 100$ ensemble members, for each target variable, i, with all others held fixed:

$$\sigma^{\mathrm{s}}_{\mathrm{ET}}(i) = \sqrt{\frac{1}{\mathrm{BN}} \sum_{b=1}^{B} \sum_{n=1}^{N} [E^*_{\mathrm{kb}}(\mathbf{s}_n, i) - \overline{E}^*_{k \cdot i}]^2}, \tag{1}$$

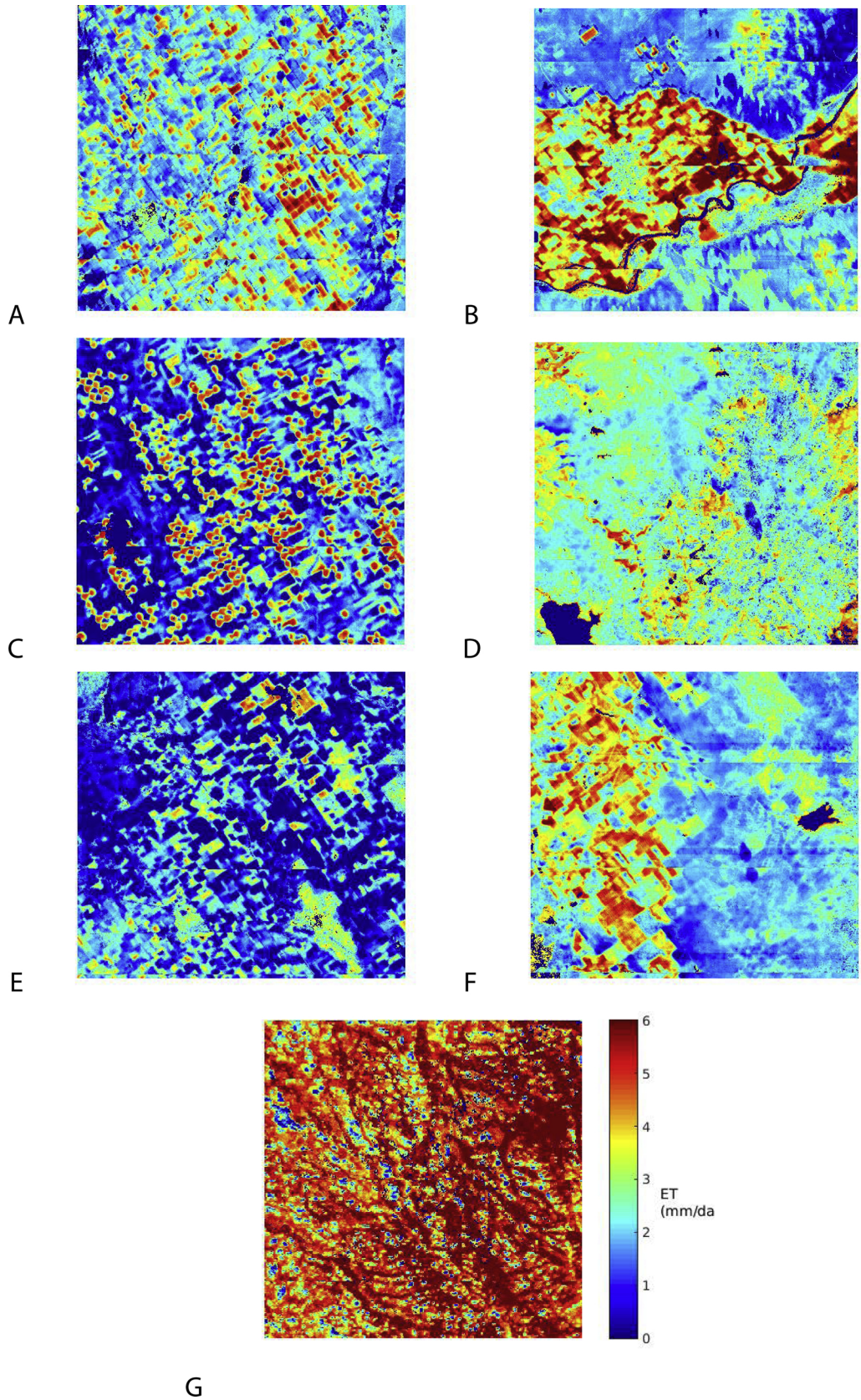

Fig. 1. From left to right, top to bottom, ET calculated by disALEXI for scenes A–G.

Table 3
Empirical standard deviations of ET for the sensitivity study. For each scene, the variable with the highest standard deviation is highlighted in italics. Note that ALEXI ET equals the aggregated ET by design, and is therefore not considered.

Scene	VZ	AT	Alb	Ins	Ins-avg	LAI	LST	NDVI	Wind
A	0.02	0.02	0.21	0.02	0.01	*0.17*	0.13	0.04	0.02
B	0.02	0.007	0.27	0.002	0.04	0.33	*0.55*	0.02	0.02
C	0.01	0.01	0.12	0.01	0.005	0.35	*0.92*	0.03	0.05
D	0.003	0.006	0.21	0.002	0.004	0.09	*0.44*	0.002	0.01
E	0.02	0.01	0.20	0.02	0.03	0.31	*0.63*	0.01	0.01
F	0.003	0.003	0.18	0.003	0.01	0.11	*0.41*	0.01	0.01
G	0.04	0.02	0.10	0.02	0.01	0.31	*0.93*	0.01	0.03

Table 4
Empirical correlations between ET and the target variable for the sensitivity study. For each scene, the variable with the highest absolute value is highlighted in italics. Note that ALEXI ET equals the aggregated ET by design, and is therefore not considered.

Scene	VZ	AT	Alb	Ins	Ins-avg	LAI	LST	NDVI	Wind
A	−0.07	−0.06	−0.43	−0.19	−0.20	0.43	*−0.83*	0.37	−0.05
B	0.12	0.26	−0.55	−0.20	−0.20	0.73	*−0.74*	0.55	−0.16
C	0.20	−0.17	−0.25	−0.17	−0.17	0.22	*−0.56*	0.29	0.20
D	0.003	−0.01	−0.26	0.05	0.02	*0.45*	−0.24	0.26	0.01
E	−0.02	−0.08	−0.26	−0.08	−0.12	0.16	*−0.51*	0.29	−0.14
F	−0.47	0.41	−0.44	−0.33	−0.40	0.69	*−0.72*	0.59	−0.47
G	−0.28	−0.28	−0.20	0.26	0.24	0.44	*−0.58*	0.23	0.12

$$\overline{E}^*_{k\cdot i} = \frac{1}{\mathrm{BN}} \sum_{b=1}^{B} \sum_{n=1}^{N} E^*_{\mathrm{kb}}(\mathbf{s}_n, i). \tag{2}$$

For each experiment the empirical correlation coefficient of the target variable with ET was calculated. Results are shown in Table 4:

$$\rho^{\mathrm{s}}_{\mathrm{ET}}(i) = \frac{\frac{1}{\mathrm{BN}} \sum_{b=1}^{B} \sum_{n=1}^{N} [E^*_{\mathrm{kb}}(\mathbf{s}_n, i) - \overline{E}^*_{k\cdot i}][X^*_{\mathrm{kbi}}(\mathbf{s}_n, i) - \overline{X}^*_{k\cdot i}]}{\sigma^{\mathrm{s}}_{\mathrm{ET}}\ \sigma^{\mathrm{s}}_i}, \tag{3}$$

where

$$\sigma^{\mathrm{s}}_i = \sqrt{\frac{1}{\mathrm{BN}} \sum_{b=1}^{B} \sum_{n=1}^{N} [X^*_{\mathrm{kbi}}(\mathbf{s}_n, i) - \overline{X}^*_{k\cdot i}]^2}, \tag{4}$$

$$\overline{X}^*_{k\cdot i} = \frac{1}{\mathrm{BN}} \sum_{b=1}^{B} \sum_{n=1}^{N} X^*_{\mathrm{kbi}}(\mathbf{s}_n, i). \tag{5}$$

In both tables, land surface temperature has the greatest effect on ET. Other variables that stand out are leaf area index and albedo. This is sensible, since disALEXI was specifically designed to take advantage of land surface temperature, and the LAI is used to partition the soil and canopy for the two-source energy balance equation.

6.2. Full uncertainty quantification

The goal of full uncertainty quantification is to characterize the probability distribution of the retrieved spatial field of ET, especially its relation to true ET. In principle, this means characterizing the N-dimensional distributions that describe the entire spatial field. Here, however, the analysis will be limited to individual distributions of ET at each pixel separately. The analysis of inter-pixel relationships required to quantify the distribution of the field as a whole is the subject of ongoing research.

Since traditional remote sensing reports errors in terms of accuracy and precision, which assumes an underlying Gaussian distribution, the purposes of this uncertainty quantification experiment are to test whether the distribution of retrieved ET values is in fact Gaussian, and if not, offer alternative ways of representing uncertainty, instead of using accuracy and precision.

The full uncertainty quantification experiment is depicted in Fig. 5. It illustrates the following steps, which are applied to each scene, k = A, B, C, D, E, F, G.

1. Simulate $B = 100$ synthetic spatial fields of input variables, $\mathbf{X}^*_{\mathrm{kb}}$, $b = 1, \ldots, 100$ from $\mathbf{X}_{k0}$, as described in Section A.2.
2. For $b = 1, \ldots, B = 100$, apply disALEXI to $\mathbf{X}^*_{\mathrm{kb}}$ to obtain corresponding synthetic fields of ET, $\mathbf{E}^*_{\mathrm{kb}}$, $b = 1, \ldots, 100$.
3. Apply disALEXI to the parent field of inputs, $\mathbf{X}_{k0}$, to obtain the "true" ET field, $\mathbf{E}_{k0}$.
4. For $b = 1, \ldots, B = 100$, calculate the difference field,

$$\boldsymbol{\Delta}_{\mathrm{kb}} = \mathbf{E}^*_{\mathrm{kb}} - \mathbf{E}_{k0}.$$

The ensemble $E^*_{\mathrm{kb}}(\mathbf{s}_n)$, $b = 1, \ldots, B = 100$ is an empirical approximation to the probability distribution of the retrieved ET at pixel $\mathbf{s}_n$ in scene k. Averaging over the B replicates at pixel $\mathbf{s}_n$ yields and subtracting the parent value at pixel $\mathbf{s}_n$ gives the pixel bias, $\bar{\Delta}_k(\mathbf{s}_n)$, and doing so for all pixels gives the bias field,

$$\bar{\boldsymbol{\Delta}}_k = (\bar{\Delta}_k(\mathbf{s}_1), \ldots, \bar{\Delta}_k(\mathbf{s}_N))', \quad \bar{\Delta}_k(\mathbf{s}_n) = \frac{1}{B} \sum_{b=1}^{B} \Delta_{\mathrm{kb}}(\mathbf{s}_n). \tag{6}$$

Since $\Delta_k(\mathbf{s}_n)$ can only be normal if $\mathbf{E}^*_{\mathrm{kb}}$ is normal, the Kolmogorov-Smirnoff test was used at 5% significance level to test the null hypothesis,

$$H_0\colon \Delta_k(\mathbf{s}_n) \sim \mathrm{Gau}(\bar{\Delta}_k(\mathbf{s}_n), \hat{\sigma}_{\Delta k}(\mathbf{s}_n)),$$

where

$$\hat{\sigma}_{\Delta k}(\mathbf{s}_n) = \frac{1}{B} \sum_{b=1}^{B} [\Delta_{\mathrm{kb}}(\mathbf{s}_n) - \bar{\Delta}_k(\mathbf{s}_n)]^2, \tag{7}$$

for each $\mathbf{s}_n$, $n = 1, \ldots, N$ and k = A, B, C, D, E, F, G. There were *no* pixels in scenes A, B, D, F, or G that were determined to be Gaussian. To illustrate, typical results, Fig. 2 shows smoothed histograms of Δ_{kb}, $b = 1, \ldots, B = 100$, for three representative pixels in Scene A. In Scenes C and D, 1.2 and 2.7 percent of the pixels were found to be Gaussian, respectively.

The vast majority of pixels in all scenes are non-Gaussian, so it makes sense to summarize the bias distributions using quantiles rather than accuracies and precisions. Fig. 3 shows six images for Scene C. The upper-left is the bias for reference. Bias values are all in the range ±1.5 mm/day, which is high for a low-ET scene. This represents relative errors of up to 25% of the average parent value of ET over all pixels in $\mathbf{E}_0$:

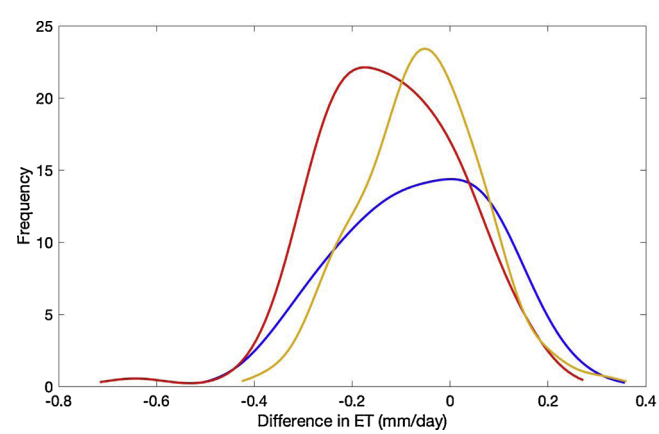

Fig. 2. Smoothed histograms of differences, $\Delta_{\mathrm{Ab}}(\mathbf{s}_n)$, $b = 1, \ldots, B$, for three typical pixels ($\mathbf{s}_n$ choices) in Scene A.

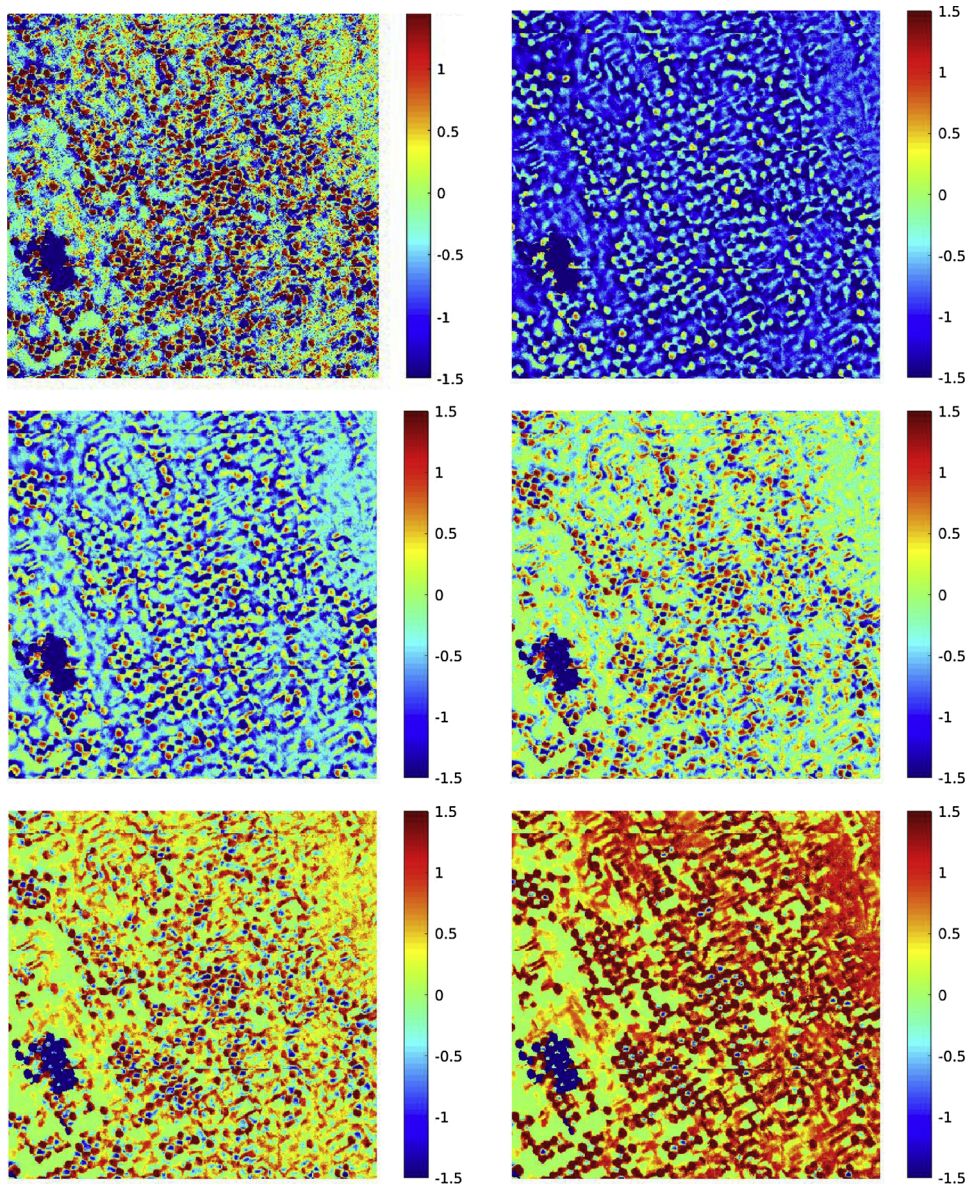

Fig. 3. From left to right, top to bottom, the mean difference ET (bias), and the 5th, 25th, 50th, 75th, and 95th percentiles of the difference image (not normalized), in mm/day, for image C.

$$\overline{E}_{k0} = \frac{1}{N}\sum_{n=1}^{N} E_{k0}(\mathbf{s}_n).$$

The remaining five images are quantile fields for the 5th, 25th, 15th, 75th, and 95th quantiles of the ensemble of B values at each pixel. Let the αth quantile of $\{\Delta_{k1}(\mathbf{s}_n), \ldots, \Delta_{\mathrm{kB}}(\mathbf{s}_n)\}$ be,

$$q_\alpha(\Delta_k(\mathbf{s}_n)) = \mathrm{argmin}_x \sum_{b=1}^{B} \frac{\mathcal{I}[\Delta_{\mathrm{kb}}(\mathbf{s}_n) \le x]}{B} \ge \alpha, \tag{8}$$

Define the αth quantile field as for scene k as,

$$\mathbf{q}_\alpha(\boldsymbol{\Delta}_k) = (q_\alpha(\Delta_k(\mathbf{s}_1)), \ldots, q_\alpha(\Delta_k(\mathbf{s}_N)))', \tag{9}$$

and the scene average as,

$$\bar{q}_{\alpha k} = \frac{1}{N}\sum_{n=1}^{N} q_\alpha(\Delta_k(\mathbf{s}_n)). \tag{10}$$

The five quantile maps in Fig. 3 (upper-right panel, and all remaining panels) show the αth quantiles fields for Scene C. Note that the bias and median fields look quite different, confirming that there are large numbers of pixels with skewed (non-Gaussian) distributions. Table 5 summarizes the result of this analysis (in mm/day) for all scenes. The bias and quantile values shown are averages, over all pixels in the scene, expressed as percentages of $\overline{E}_{k0}$.

Table 5 shows that the majority of scenes have biases close to zero, with the 75th quantile within $\sim \pm 15\%$ of parent ET, and the 95th quantile within $\sim \pm 30\%$ of parent ET. The notable exceptions are the two low-ET scenes, C and E. In these cases, the quantiles of the bias values are much higher. Even when the normalization step is removed (see Fig. 4), scenes C and E have a higher (absolute) ET difference than the higher-ET datasets (scenes A, B, D, F, and G). Datasets C and E are also not centered at zero, with the simulated dataset outputs producing higher mean ET values than the original (negative bias), by approximately 10%.

In Fig. 3, one can see the structure in the quantiles. In the higher quantiles, the irrigated fields are highlighted. In the lower quantiles, the spaces between the pivot irrigation are seen. There is a particular section (bottom far left) where the irrigated fields have lower values in all quantiles, but in general, the irrigated fields follow the same spatial pattern in all quantiles, in that the fields have higher uncertainty values

Table 5
The normalized bias and quantiles expressed percentages of the average value of ET in the parent scene.

k	$100 \times \bar{E}_{k0}$	$100 \times \tilde{\Delta}_k/\bar{E}_{k0}$	$100 \times \bar{q}_{0.05k}/\bar{E}_{k0}$	$100 \times \bar{q}_{0.25k}/\bar{E}_{k0}$	$100 \times \bar{q}_{0.50k}/\bar{E}_{k0}$	$100 \times \bar{q}_{0.75k}/\bar{E}_{k0}$	$100 \times \bar{q}_{0.95k}/\bar{E}_{k0}$
A	2.41	4.04	−17.20	−3.49	4.12	11.78	24.81
B	2.70	0.49	−36.13	−14.22	0.93	14.45	36.92
C	1.70	−9.29	−98.77	−41.77	−11.40	22.25	87.78
D	2.60	−1.52	−30.29	−10.74	−0.97	8.02	27.86
E	1.21	−5.85	−93.78	−41.67	−12.36	28.92	94.94
F	2.52	−3.21	−31.75	−12.09	−3.37	5.49	26.68
G	4.87	−0.26	−34.42	−8.11	2.62	11.16	24.21

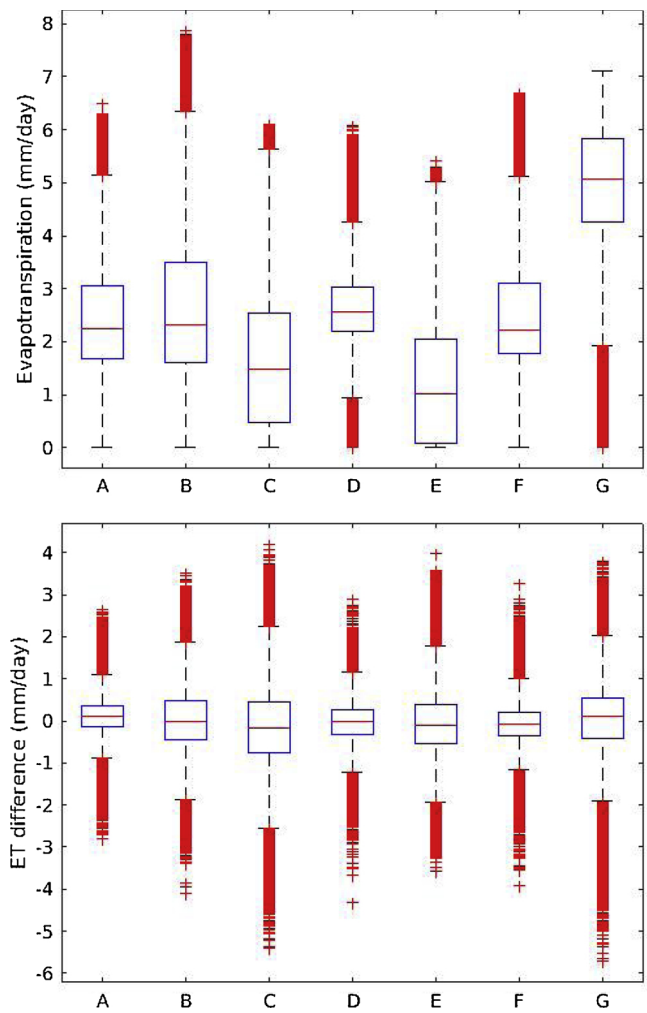

Fig. 4. Distribution of (top) the original ET values for each scene, and (bottom) the distributions of pixel biases (unnormalized) for each scene, in mm/day. The center line is the median, and the outer edges of the box represent the 25th and 75th percentiles, respectively. The red + marks represent values outside the 1st and 99th percentiles. (For interpretation of the references to color in this figure legend, the reader is referred to the web version of this article.)

than the background.

Fig. 4 shows the raw ET values for each scene, as well as the raw bias in each scene (unnormalized). Scenes C and E have low ET values, but comparable biases to the other scenes, which is a higher proportion of parent ET than expected. Despite the scene differences (such as spatial location, landcover type, meteorological conditions), none of these had any apparent effect on the biases represented by the quantiles. Fig. 4 shows the differences per scene in mm/day.

7. Discussion

Here, a model is proposed that exploits the internal statistical variability of the data themselves through simulation, and quantifies uncertainty through simulated probability distributions of the quantities of interest. Land surface temperature (LST) is the leading driver of uncertainty in disALEXI ET, although albedo and leaf area index (LAI) are important as well. In addition, the per-pixel distributions of ET are almost universally non-Gaussian. This means that precision and accuracy are *not* adequate metrics to describe uncertainty, so quantiles may be more beneficial in order to summarize the distributions of ET. It also means that it is not possible to use simple linear error propagation to quantify the effects of changes in inputs on disALEXI output.

The bias of the ET estimates is consistent across five different scenes, and generally robust to changes in inputs across geophysical conditions. The biases for scenes A, B, D, F, and G are generally within about four percent of the true ET values in these simulations. The two scenes with low ET (scenes C and E), showed higher (absolute) bias. Since the ET values are lower, one might expect a lower raw bias (unnormalized), since ET error is thought to be proportional to value, and is usually expressed as a percentage. However, Fig. 4 shows that this is not the case.

For scenes A, B, D, F, and G, in the 75th quantile, the values of $100 \times \bar{q}_{.75k}/\bar{E}_{k0}$, are within 15% of the parent ET value (see Table 5). The scenes with low ET (scenes C and E), showed higher deviations (75th quantile showed values up to 30% of the parent ET). This is true for all quantiles.

Note the similarities in all the quantiles for scenes A, B, D, F, and G, as well as the overestimation of low ET (scenes C and E). The 75th quantile of the bias of ET is within 15% of the parent value. This is slightly higher than the 10% derived from validation, as seen in other ET models using ECOSTRESS. This reflects the difference between uncertainty quantification and validation; overall the uncertainty was higher than observed in validation studies.

8. Conclusion

In this manuscript, a method for quantifying sensitivity and uncertainty in retrievals of ET from remote sensing data acquired by ECOSTRESS was introduced. A single month of data was used to illustrate this method, by way of introduction. While this should not be considered representative of all input data combinations, the variability seen was indicative of the expected uncertainty during summer months in North America. The method fits and then simulates from a spatial-statistical model of the ET field and its inputs. Crucially, variable-to-variable, spatial, and cross-variable-spatial relationships are maintained. While this method is general and could be applied to data from other remote sensing instruments, it has been used here to evaluate the performance of the disALEXI ET model retrieval for ECOSTRESS.

An important note is the distinction between validation (comparison with field data), verification (comparison with other models) and

uncertainty quantification. Here, uncertainty quantification is defined to be the variability of the output of the disALEXI model, when all inputs are varied in a way that is reasonable. Here, the reasonable input variation is taken from the data itself, and the structure of the data is maintained.

Uncertainty is vital because (a) it is needed for robust scientific investigation in order to separate hypotheses, (b) it is vital for risk assessment, and (c) because it has been lacking in past investigations. Uncertainty may be used by modelers and users in the agricultural and water resource communities.

It was found that scene-based ET uncertainty is generally less than 1 mm day and frequently less than 0.3 mm day. The uncertainty is not Gaussian, and is not well described using metrics such as accuracy and precision. It is the authors' recommendation that uncertainty be presented as a range of values with an associated confidence interval.

Authors' contribution

Kerry Cawse-Nicholson: conceptualization; methodology; software; formal analysis; investigation; data curation; writing – original draft; writing – review and editing; visualization.

Amy Braverman: conceptualization; methodology; formal analysis; investigation; writing – original draft; writing – review and editing.

Emily L. Kang: conceptualization; methodology; formal analysis; investigation; writing – original draft; writing – review and editing.

Miaoqi Li: conceptualization; methodology; software; formal analysis; investigation; data curation; writing – original draft; writing – review and editing; visualization.

Margaret Johnson: methodology; formal analysis; investigation; writing – review and editing.

Gregory Halverson: methodology; formal analysis; investigation; writing – review and editing.

Martha Anderson: methodology; writing – original draft; writing – review and editing.

Christopher Hain: methodology; writing – original draft; writing – review and editing.

Michael Gunson: supervision; funding; writing – review and editing.

Simon Hook: supervision; funding; writing – review and editing.

Conflict of interest

None declared.

Acknowledgements

This work was supported by JPL's Advanced Concept funding Part of the research described in this paper was carried out at the Jet Propulsion Laboratory, California Institute of Technology, under contract with the National Aeronautics and Space Administration. © 2019 California Institute of Technology. Government sponsorship acknowledged.

Appendix A

A.1 Statistical model

Let the parent spatial field be denoted by the $N \times M$ matrix $\mathbf{X}_0$ where N is the number of pixels in the field and $M = 12$ is the number of inputs to the disALEXI model of ET (see Table 1). Let $\mathbf{s}$ be a point location that represents a pixel center (e.g., latitude and longitude), and let $\mathbf{X}_0(\mathbf{s}_n)$ be the parent data set's vector of input values at the nth pixel: $\mathbf{X}_0(\mathbf{s}_n) = (X_{0,a}(\mathbf{s}_n), ..., X_{0,M}(\mathbf{s}_n))'$ where $(\cdot)'$ indicates vector (or matrix) transpose. Then, $\mathbf{X}_0 = \{\mathbf{X}_0(\mathbf{s}_n)\}$, $n = 1, ..., N$ represents the set of M inputs over the entire field.

The model will treat certain input variables jointly since Albedo, LST, LAI, and NDVI are known to be correlated (set 1), and Insolation and Daily mean insolation (set 2) are obviously correlated. Each of the remaining variables is a member of its own set (sets 3–8). All variables are assumed correlated within their set, but uncorrelated with anything that is not. So, $M = \sum_{j=1}^{8} m_j$, where m_j is the number of variables in set j: $m_1 = 4$, $m_2 = 2$, and $m_j = 1$ for $j = 3, d, 5, 6, 7, 8$. Next, the machinery for simulating spatial fields using correlated sets of variables may be developed.

Each of the pixels represented by $\mathbf{X}_0$ contains an M-dimensional vector that is the sum of the "true" vector of ET predictors, $\mathbf{Y}_0(\mathbf{s}_n)$, plus error $\varepsilon(\mathbf{s}_n)$:

$$\mathbf{X}_0(\mathbf{s}_n) = \mathbf{Y}_0(\mathbf{s}_n) + \varepsilon(\mathbf{s}_n), \tag{11}$$

where $\varepsilon(\mathbf{s}_n) = (\varepsilon_1(\mathbf{s}_n), ..., \varepsilon_M(\mathbf{s}_n))' \sim \mathcal{N}(\mathbf{0}, \mathbf{m}\Sigma_\varepsilon)$ is a vector of white noise measurement errors with an $M \times M$ diagonal covariance matrix $\mathbf{m}\Sigma_\varepsilon$ whose diagonal elements are $\{\sigma^2_{\varepsilon,i}\}$, $i = 1, ..., M$. The elements in the random vector $\mathbf{m}\varepsilon(\mathbf{s}_n)$ are called the nugget effect in spatial statistics and can be estimated by fitting empirical semivariograms near the origin as suggested in Kang et al. (2010).

Here the "true" value of the ith element of predictor vector at location $\mathbf{s}_n$ is modeled as,

$$Y_{0,i}(\mathbf{s}_n) = (\mathbf{T}_i(\mathbf{s}_n))'\boldsymbol{\beta}_i + (\mathbf{S}_i(\mathbf{s}_n))'\boldsymbol{\eta}_i + \xi_i(\mathbf{s}_n). \tag{12}$$

where $\mathbf{T}_i(\mathbf{s}_n)$ is a $p_i \times 1$ vector of covariates and $(\mathbf{T}_i(\mathbf{s}_n))'\mathbf{m}\beta_i$ models the large-scale spatial trend in the data. The term $(\mathbf{S}_i(\mathbf{s}_n))'\mathbf{m}\eta_i$ harkens back to the spatial random effects (SRE) model described in Cressie and Johannesson (2008), where $\mathbf{S}_i(\mathbf{s}_n)$ is specified by a set of r_i ($r_i \ll N$) multi-resolution spatial basis functions and the r_i-dimensional random vector $\mathbf{m}\eta_i \sim N(\mathbf{0}, \mathbf{K}_i)$. This SRE component describes the *small-scale* contribution to $Y_{0,i}(\mathbf{s}_n)$. It facilitates efficient computation because it provides a low-rank representation of small-scale behavior. The third term on the right-hand-side of Eq. (12) is the *fine-scale* term suggested in Ma et al. (2019) and Ma and Kang (2019). It assumes that $\mathbf{m}\xi_i \equiv (\xi_i(\mathbf{s}_1), ..., \xi_i(\mathbf{s}_N))'$ follows a spatial conditional autoregressive (CAR) model:

$$\boldsymbol{\xi}_i \sim \mathcal{N}(\mathbf{0}, \boldsymbol{\Sigma}_{\mathrm{CAR},i}), \quad \mathbf{Q}_i = \mathbf{m}\Sigma^{-1}_{\mathrm{CAR},i} = (\mathbf{I} - \gamma_i\mathbf{H}_i)/\tau_i^2, \tag{13}$$

where τ_i^2 represent the conditional variance of a single element in $\mathbf{m}\xi$ given all the other elements; $\mathbf{H}_i$ is an $N \times N$ matrix specified according to the neighborhood structure in the lattice over the field; γ_i denotes the spatial dependence parameter; when $\gamma_i = 0$, the elements in $\mathbf{m}\xi_i$ becomes spatially independent. This model given by Eq. (12) is called the *fused Gaussian process* (FGP) (Ma et al., 2019). Eqs. (12) and (13) specify the FGP model for an individual input variable. Next, dependence across input variables is introduced.

The FGP model is defined for a univariate spatial process corresponding to $m_j = 1$. It is extended here to model a general m-variate spatial process. For illustration in this manuscript, the model is presented for a bivariate process with $m = 2$. Extension to larger values of m, including

$m = m_j = 4$ for some j, is straightforward. As in Ma and Kang (2019), it is assumed that $\mathbf{m}\eta_i$ and $\mathbf{m}\xi_i$ are independent for the ith input, but introduce cross-dependence by modeling the joint distribution of $(\mathbf{m}\eta_1, \mathbf{m}\eta_2)$ and $(\mathbf{m}\xi_1, \mathbf{m}\xi_2)$, respectively, which induces spatial dependence across the $m = 2$ inputs. In particular, it is assumed that:

$$\begin{pmatrix} \mathbf{m}\eta_1 \\ \mathbf{m}\eta_2 \end{pmatrix} \sim N(\mathbf{0}, \mathbf{K}) \quad \text{with} \quad \mathbf{K} = \begin{pmatrix} \mathbf{K}_1 & \mathbf{K}_{12} \\ \mathbf{K}_{12}' & \mathbf{K}_2 \end{pmatrix}; \tag{14}$$

that is, $\mathbf{m}\eta_1$ and $\mathbf{m}\eta_2$ are jointly normal with a $(r_1 + r_2) \times (r_1 + r_2)$ covariance matrix $\mathbf{K}$. As suggested in Cressie and Johannesson (2008) and Nguyen et al. (2012), no further parameterization of this matrix $\mathbf{K}$ is assumed, besides requiring it to be positive definite so that this joint distribution can be flexible enough to describe spatial dependence that is potentially nonstationary.

To model $(\mathbf{m}\xi_1, \mathbf{m}\xi_2)$, assume the following multivariate CAR model:

$$\begin{pmatrix} \mathbf{m}\xi_1 \\ \mathbf{m}\xi_2 \end{pmatrix} \sim N(\mathbf{0}, \mathbf{m}\Sigma_\xi) \quad \text{with } \mathbf{m}\Sigma_\xi = \mathbf{m}\Gamma \otimes \mathbf{Q}^{-1}, \tag{15}$$

where

$$\mathbf{m}\Gamma = \begin{pmatrix} 1 & \rho \\ \rho & 1 \end{pmatrix} \quad \text{and} \quad \mathbf{Q} = (\mathbf{I} - \gamma\mathbf{H})/\tau^2.$$

Here, the $(2N) \times (2N)$ covariance matrix $\mathbf{m}\Sigma_\xi$ takes a separable form as a Kronecker produce of a 2×2 correlation matrix with ρ representing the correlation across inputs, and the $N \times N$ spatial covariance matrix induced by a CAR model in which γ is the spatial dependence parameter and τ^2 is the conditional variance. This model for $\mathbf{m}\xi$ includes a small number of parameters and the resulting Kronecker form also enables efficient computation for parameter estimation and simulation. In addition, although the covariance matrix of $(\mathbf{m}\xi_1, \mathbf{m}\xi_2)$ has the separable form, the covariance matrix of the inputs are induced by both $(\mathbf{m}\eta_1, \mathbf{m}\eta_2)$ and $(\mathbf{m}\xi_1, \mathbf{m}\xi_2)$ and thus is not necessarily separable. Despite this, this multivariate CAR model is just one possible formulation and there are possible alternative modeling strategies.

Combining and simplifying Eqs. (11), (12), (14), and (15) using matrix notation:

$$\text{vec}(\mathbf{X}_0) = \mathbf{T}\mathbf{m}\beta + \mathbf{S}\mathbf{m}\eta + \mathbf{m}\xi + \mathbf{m}\varepsilon, \tag{16}$$

where

$$\mathbf{T} = \begin{pmatrix} \mathbf{T}_1 & \mathbf{0} \\ \mathbf{0} & \mathbf{T}_2 \end{pmatrix}, \quad \mathbf{m}\beta = \begin{pmatrix} \mathbf{m}\beta_1 \\ \mathbf{m}\beta_2 \end{pmatrix};$$

$$\mathbf{S} = \begin{pmatrix} \mathbf{S}_1 & \mathbf{0} \\ \mathbf{0} & \mathbf{S}_2 \end{pmatrix}, \quad \mathbf{m}\eta = \begin{pmatrix} \mathbf{m}\eta_1 \\ \mathbf{m}\eta_2 \end{pmatrix}, \quad \mathbf{m}\xi = \begin{pmatrix} \mathbf{m}\xi_1 \\ \mathbf{m}\xi_2 \end{pmatrix}, \quad \mathbf{m}\varepsilon = \begin{pmatrix} \mathbf{m}\varepsilon_1 \\ \mathbf{m}\varepsilon_2 \end{pmatrix}.$$

Here, $\mathbf{m}\varepsilon_i = (\varepsilon_i(\mathbf{s}_1), \ldots, \varepsilon_i(\mathbf{s}_N))'$ for $i = 1, 2$; $\mathbf{T}_i$ is the $N \times p_i$ matrix whose rows are given by $\mathbf{T}_i(\mathbf{s}_n)'$, $n = 1, \ldots, N$, for $i = 1, 2$. Similarly, $\mathbf{S}_i$ is the $N \times r_i$ matrix whose rows are given by $\mathbf{S}_i(\mathbf{s}_n)'$, $n = 1, \ldots, N$, for $i = 1, 2$.

The model description above is general and can be extended for $m > 2$. Specifically, for example, when $m = 3$, the matrix $\mathbf{m}\Gamma$ will be the 3×3 correlation with all off-diagonal elements being ρ, and so on for $m = 4$ and higher. When $m = 1$ the m-variate FGP model reduces to the univariate FGP and is a special case. The model is flexible enough to allow for different covariates $\mathbf{T}_i(\cdot)$ and basis functions $\mathbf{S}_i(\cdot)$ for $i = 1, \ldots, m$.

The m-variate FGP model is fitted to the first set of the input variables in Table 1 (Albedo, LST, LAI, and NDVI, $i = 1, b, c, 4$, $m_1 = 4$) because of known physical relationships between vegetation fraction, temperature and albedo. The same is done for Insolation and Daily solar insolation, $i = 5, 6$, $m_2 = 2$) for which the correlation coefficient is above 0.9. Three of the remaining six inputs variables are modeled individually (i.e., $m = 1$ for $i = 7, 8, 9$, $m_j = 1$ for $j = 3, 4, 5$) using univariate FGP. The remaining three input variables, Elevation and land cover are set to the parent data set values and are not simulated because they are thought to not change during the time window under consideration. ALEXI ET is not simulated because there is an enforced relationship between the final ET and ALEXI ET (since the sum of the fine resolution pixels is enforced to equal the relevant coarse resolution pixel).

For each ECOSTRESS scene described in Section 5, six FGP models are fit, one for each variable set, $j = 1, \ldots, 5$. Denote these by,

$$\text{FGP}(\widehat{\mathbf{m}\beta}_{(j)}, \widehat{\mathbf{K}}_{(j)}, \hat{\rho}_{(j)}, \underset{(j)}{\hat{\tau}^2}, \hat{\gamma}_{(j)}; \mathbf{T}_{(j)}, \mathbf{S}_{(j)}), \quad j = 1, \ldots, 5, \tag{17}$$

where subscript (j) is included in the notations to highlight that the model parameters such as large-scale and small-scale basis functions $(\mathbf{T}_{(j)}, \mathbf{S}_{(j)})$ may differ across the five models, $j = 1, \ldots, 5$. The dimensions of the parameters $\widehat{\mathbf{m}\beta}_{(j)}$ and $\widehat{\mathbf{K}}_{(j)}$ are conformable with the with the corresponding basis functions, and hats indicated that the parameter values are maximum-likelihood estimates. These are obtained via the expectation-maximization (EM) algorithm applied to data in the scene.

Multi-resolution local bisquare basis functions (Nguyen et al., 2012) are used for both $\mathbf{T}_{(j)}$ and $\mathbf{S}_{(j)}$. The basis functions corresponding to coarse spatial scales are used for $\mathbf{T}_{(j)}$, and those for finer scales are used for $\mathbf{S}_{(j)}$ as in Shi and Cressie (2007). Local spatial structure is modeled by the proximity matrix $\mathbf{H}$. This assumes on the first-order neighborhood structure, which is the simplest model possible and is used in Ma et al. (2019), Ma and Kang (2019). The fitting procedure (estimation of the parameters using EM) is computationally feasible for data sets of the size of ECOSTRESS scenes because of the low-rank representation $\mathbf{S}\mathbf{m}\eta$ and the sparse matrix $\mathbf{Q}$. The FGP model has been validated and demonstrated in Ma and Kang (2019) and Li et al. (2019), and readers are referred there for further information.

A.2 Simulation

Each of the six FGP models fitted in the previous section defines a probability distribution from which one can simulate all the input values. To do so, execute the following steps:

1. Simulate B, 4-variate spatial fields of Albedo, NDVI, LAI, and LST: $\mathbf{X}_{(1),b} \sim \text{FGP}(\widehat{\mathbf{m}\beta}_{(1)}, \widehat{\mathbf{K}}_{(1)}, \hat{\rho}_{(1)}, \hat{\tau}^2_{(1)}, \hat{\gamma}_{(1)}; \mathbf{T}_{(1)}, \mathbf{S}_{(1)}), b = 1, \ldots, B$. Note that although these B 4-variate fields are generated independently, they follow the same multivariate spatial distribution and incorporate dependence over the space and across the four inputs.
2. Simulate B, bivariate spatial fields of Insolation and Daily mean insolation: $\mathbf{X}_{(2),b} \sim \text{FGP}(\widehat{\mathbf{m}\beta}_{(2)}, \widehat{\mathbf{K}}_{(2)}, \hat{\rho}_{(2)}, \hat{\tau}^2_{(2)}, \hat{\gamma}_{(2)}; \mathbf{T}_{(2)}, \mathbf{S}_{(2)}), b = 1, \ldots, B$.
3. Simulate B, univariate spatial fields of Wind speed, Air temperature, and View angle: $X_{(j),b} \sim \text{FGP}(\widehat{\mathbf{m}\beta}_{(j)}, \widehat{\mathbf{K}}_{(j)}, \hat{\rho}_{(j)}, \hat{\tau}^2_{(j)}, \hat{\gamma}_{(j)}; \mathbf{T}_{(j)}, \mathbf{S}_{(j)}), b = 1, \ldots, B$; $j = 3, 4, 5$.
4. Create B copies of the parent spatial field for ALEXI ET $\mathbf{X}_{(6),b}$, B copies of the parent spatial field for Elevation, $\mathbf{X}_{(7),b}$, and B copies of the parent spatial field for Landcover, $\mathbf{X}_{(8),b}$, $b = 1, \ldots, B$.
5. For $b = 1, \ldots, B$, create a 12-variate vector of simulated predictors in each pixel,

$$\begin{aligned}\mathbf{X}_b(\mathbf{s}_n) &= [(\mathbf{X}_{(1),b}(\mathbf{s}_n))', (\mathbf{X}_{(2),b}(\mathbf{s}_n))', X_{(3),b}(\mathbf{s}_n), X_{(4),b}(\mathbf{s}_n),\\ &\quad X_{(5),b}(\mathbf{s}_n), X_{(6),b}(\mathbf{s}_n), X_{(7),b}(\mathbf{s}_n), X_{(8),b}(\mathbf{s}_n)]'.\end{aligned} \tag{18}$$

6. Denote the bth simulated spatial field by $\mathbf{X}_b$,

$$\mathbf{X}_b = ((\mathbf{X}_b(\mathbf{s}_1))', \ldots, (\mathbf{X}_b(\mathbf{s}_N))')'. \tag{19}$$

To simulate a spatial field from the model $\text{FGP}(\mathbf{m}\beta, \mathbf{K}, \rho, \tau^2, \gamma; \mathbf{T}, \mathbf{S})$, perform the following steps:

1. Simulate an r-dimensional vector $\mathbf{m}\zeta_1 \sim N(\mathbf{0}, \mathbf{I})$;
2. Simulate an (mN)-dimensional vector $\mathbf{m}\zeta_2 \sim N(\mathbf{0}, \mathbf{I})$;
3. Simulate an (mN)-dimensional vector $\mathbf{m}\zeta_3 \sim \mathcal{N}(\mathbf{0}, \mathbf{I})$;
4. Compute the Cholesky decomposition of the low-dimensional $r \times r$ matrix $\mathbf{K}$ with $r = \sum_{i=1}^{m} r_i$ such that $\mathbf{K} = \mathbf{F}\mathbf{F}'$.
5. Compute the Cholesky decomposition of the low-dimensional $m \times m$ matrix $\mathbf{m}\Gamma$ and sparse $N \times N$ matrix $\mathbf{Q}$, respectively, such that $(\mathbf{m}\Gamma)^{-1} = \mathbf{L}'\mathbf{L}$ and $\mathbf{Q} = \mathbf{R}'\mathbf{R}$.
6. Note that $\mathbf{m}\zeta_1$, $\mathbf{m}\zeta_2$, and $\mathbf{m}\zeta_3$ are simulated independently. The simulated value is calculated as $\mathbf{T}\mathbf{m}\beta + \mathbf{S}\mathbf{F}\mathbf{m}\zeta_1 + (\mathbf{L}^{-1} \otimes \mathbf{R}^{-1})\mathbf{m}\zeta_2 + \mathbf{m}\Sigma_\epsilon^{1/2}\mathbf{m}\zeta_3$ where $\mathbf{m}\Sigma_\epsilon^{1/2}$ is the diagonal matrix with all elements equal to the square roots of those in $\mathbf{m}\Sigma_\epsilon$.

The simulated spatial fields of inputs, $\mathbf{X}_b$, $b = 1, \ldots, B$, are fed to disALEXI yielding an ensemble of B univariate spatial fields of ET estimates, $\mathbf{E}^*_b$,

$$\mathbf{E}^*_b = (E^*_b(\mathbf{s}_1), \ldots, E^*_b(\mathbf{s}_N))'. \tag{20}$$

The probability distribution that describes ET uncertainty at the nth pixel is approximated by the histogram of $E^*_b(\mathbf{s}_n$ values. The simulated true ET value, $E_0(\mathbf{s}_n)$, can be located in this distribution. The extent to which it differs from the histogram mean,

$$\overline{E}^*(\mathbf{s}_n) = \frac{1}{B}\sum_{b=1}^{B} E^*_b(\mathbf{s}_n), \tag{21}$$

is a measure of bias, and width of the histogram is a measure variability. However, there is no guarantee that this distribution will be Gaussian. In fact, it is quite unlikely since disALEXI effects a non-linear transformation of its inputs. The question of how best to characterize these distributions will be addressed in Section 6.

The simulation approach also allows us to probe the spatial covariance structure of the field by computing empirical covariances between pairs of pixels, $\mathbf{s}_n$ and $\mathbf{s}_m$:

$$\text{cov}(E^*(\mathbf{s}_n), E^*(\mathbf{s}_m)) = \frac{1}{B}\sum_{b=1}^{B} (E^*(\mathbf{s}_n) - \overline{E}^*(\mathbf{s}_n))(E^*(\mathbf{s}_m) - \overline{E}^*(\mathbf{s}_m)). \tag{22}$$

Alternatively, one could fit descriptive statistics such as variograms or even parametric covariance functions, to each of the B synthetic fields to obtain estimates (and their uncertainties) of features such as correlation length, isotropy, etc.

When the 4-variate FGP model is fitted for Albedo, NDVI, LAI, and LST corresponding to $j = 1$ and $m_j = 4$), $\mathbf{T}_{(1)}$ is specified to be intercept term, local-bisquare basis functions at three resolutions (a total of $5 \times 5 + 10 \times 10 + 20 \times 20$), together with 100 basis functions chosen from Resolution 4 as suggested in Shi and Cressie (2007); $\mathbf{S}_{(1)}$ is specified to be the remaining 1500 basis functions in Resolution 4. When fitting the bivariate FGP model for Insolation and Daily mean insolation, corresponding to $j = 2$, $\mathbf{T}_{(2)}$ consists of the intercept term, the spatial x, and y coordinates and their squares, respectively, while $\mathbf{S}_{(2)}$ consists of local-bisquare basis functions from the first two resolutions, resulting a total of $5 \times 5 + 10 \times 10 = 125$ basis functions. For the univariate FGP model for wind speed ($j = 3$), $\mathbf{T}_{(3)}$ is the intercept term, the spatial coordinates and their squares, respectively. $\mathbf{T}_{(4)}$ in the univariate FGP for air temperature is specified to be the intercept and the spatial coordinates. The univariate FGP for view angle use $\mathbf{T}_{(5)}$ to be a simple linear regression function of the x-coordinate. In all the three univariate FGP models, $\mathbf{S}_{(j)}$ consists of local-bisquare basis functions from the first two resolutions, for j= 3, 4 and 5. In this work, the guidelines of specifying equally-spaced multiresolutional basis functions in Cressie and Johannesson (2008) and Shi and Cressie (2007) are followed. It is also possible to choose basis functions in a data-driven way (Tzeng and Huang, 2018; Ma and Kang, 2019), which is beyond the scope of this work. (Fig. 5).

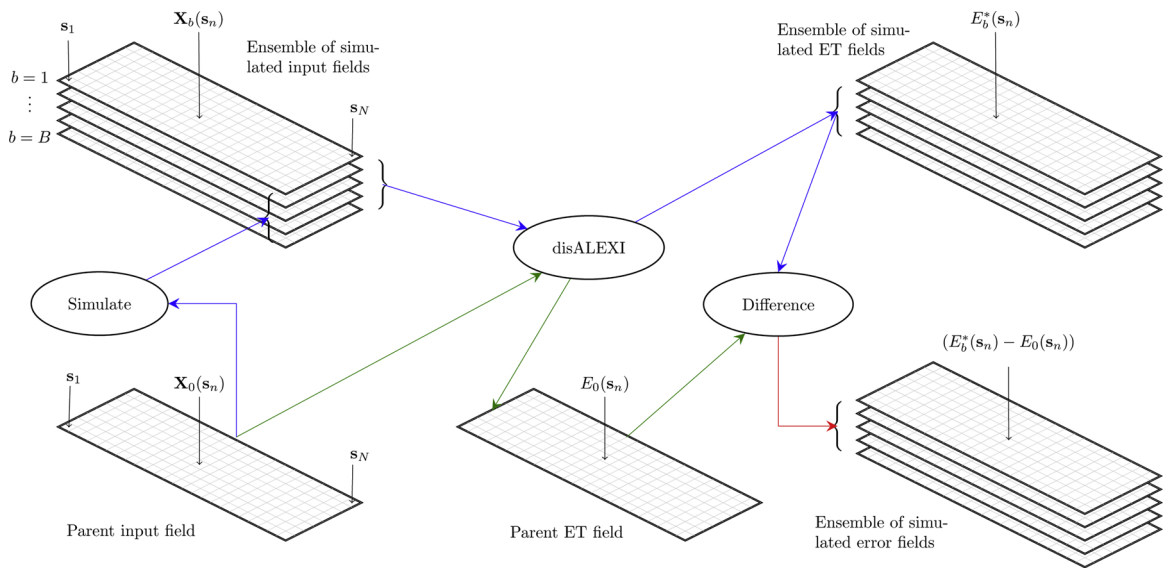

Fig. 5. Schematic diagram of uncertainty quantification methodology. The parent spatial field of inputs is in the lower-left, and the corresponding ET spatial field is in the lower-middle. The parent field is transformed into the ET field by disALEXI (green arrows). The parent input field is also the source of the stack of simulated input spatial fields in the upper-left via the spatial-statistical simulation. Each sheet in this stack in input to disALEXI to produce a corresponding sheet in the simulated ET spatial field stack in the upper-right. Finally, the parent ET field is subtracted (pixel-by-pixel) from each sheet in the simulated ET stack, yielding the stack of simulated error spatial fields in the lower-right. The blue, green, and red arrows link inputs and outputs. (For interpretation of the references to color in this figure legend, the reader is referred to the web version of this article.)

Appendix B

See Table 6

Table 6
A list of filenames used as input into the experiments conducted in this manuscript.

Scene	ECOSTRESS LST filename
A	ECOSTRESS_L2_LSTE_00870_009_20180831T185510_0501_02.h5
B	ECOSTRESS_L2_LSTE_00870_009_20180831T185510_0501_02.h5
C	ECOSTRESS_L2_LSTE_00762_007_20180824T200949_0501_02.h5
D	ECOSTRESS_L2_LSTE_00809_006_20180827T204429_0501_02.h5
E	ECOSTRESS_L2_LSTE_00809_006_20180827T204429_0501_02.h5
F	ECOSTRESS_L2_LSTE_00809_007_20180827T204521_0501_02.h5
G	ECOSTRESS_L2_LSTE_00824_013_20180828T195253_0501_02.h5

References

Allen, R.G., Tasumi, M., Trezza, R., 2007. Satellite-based energy balance for mapping evapotranspiration with internalized calibration (metric) – model. J. Irrig. Drain. Eng. 133, 380–394.

Anderson, M.C., Norman, J.M., Diak, G.R., Kustas, W.P., Mecikalski, J.R., 1997. A two-source time-integrated model for estimating surface fluxes using thermal infrared remote sensing. Rem. Sens. Environ. 60, 195–216.

Anderson, M., Norman, J., Mecikalski, J., Torn, R., Kustas, W., Basara, J., 2004. A multi-scale remote sensing model for disaggregating regional fluxes to micrometeorological scales. J. Hydrometeorol. 5, 343–363.

Anderson, M., Kustas, W., Alfieri, J., Hain, C., Prueger, J., Evett, S., Colaizzi, P., Howell, T., Chavez, J., 2012. Mapping daily evapotranspiration at landsat spatial scales during the bearex'08 field campaign. Adv. Water Resour. 50, 162–177.

Anderson, M.C., Zolin, C.A., Sentelhas, P.C., Hain, C.R., Semmens, K., Yilmaz, M.T., Gao, F., Otkin, J., Tetrault, R., 2016. The evaporative stress index as an indicator of agricultural drought in Brazil: an assessment based on crop yield impacts. Rem. Sens. Environ. 174, 82–99.

Badgley, G., Fisher, J.B., Jimenez, C., Tu, K.P., Vinukollu, R.K., 2015. On uncertainty in global evapotranspiration estimates from choice of input forcing datasets. J. Hydrometeorol. 16, 1449–1455.

Bastiaanssen, W., Menenti, M., Feddes, R., Holtslag, A., 1998. A remote sensing surface energy balance algorithm for land (SEBAL). 1. Formulation. J. Hydrol. 212–213, 198–212.

Cressie, N., Johannesson, G., 2008. Fixed rank kriging for very large spatial data sets. J. R. Stat. Soc.: Ser. B 70, 209–226.

Cressie, N.A.C., Wikle, C.K., 1993. Statistics for Spatio-Temporal Data. John Wiley and Sons, Inc.

Cressie, N.A.C., 1993. Statistics for Spatial Data, Revised Edition. John Wiley Sons, Inc.

Ershadi, A., McCabe, M.F., Evans, J.P., Mariethoz, G., Kavetski, D., 2013. A Bayesian analysis of sensible heat flux estimation: Quantifying uncertainty in meteorological forcing to improve model prediction. Water Resour. Res. 49, 2343–2358.

Fisher, J.B., Tu, K.P., Baldocchi, D.D., 2008. Global estimates of the land-atmosphere water flux based on monthly avhrr and islscp-ii data, validated at 16 fluxnet sites. Rem. Sens. Environ. 112, 901–919.

Fisher, J.B., Mallick, K., Lee, J.-H., Hulley, G.C., Hughes, C.G., Hook, S.J., 2013. Uncertainty in evapotranspiration from uncertainty in land surface temperature. American Meteorological Society.

Fisher, J.B., Melton, F., Middleton, E., Hain, C., Anderson, M., Allen, R., McCabe, M.F., Hook, S., Baldocchi, D., Townsend, P.A., Kilic, A., Tu, K., Miralles, D.D., Perret, J., Lagouarde, J.-P., Waliser, D., Purdy, A.J., French, A., Schimel, D., Famiglietti, J.S., Stephens, G., Wood, E.F., 2017. The future of evapotranspiration: Global requirements for ecosystem functioning, carbon and climate feedbacks, agricultural management, and water resources. Water Resour. Res. 53, 2618–2626.

Fisher, J.B., 2018. Level-3 Evapotranspiration L3(ET_PT-JPL) Algorithm Theoretical Basis Document. Technical Report. NASA Jet Propulsion Laboratory.

Homer, C., Dewitz, J., Yang, L., Jin, S., Danielson, P., Xian, G., Coulston, J., Herold, N., Wickham, J., Megown, K., 2015. Completion of the 2011 national land cover database for the conterminous united states – representing a decade of land cover change information. Photogram. Eng. Rem. Sens. 81, 345–353.

Hook, S., S.M, 2019. Ecostress Geolocation Daily l1b Global 70 m [Data Set].

Hulley, H.S., G.C, 2018. Ecostress Level 2 Land Surface Temperature and Emissivity Algorithm Theoretical Basis Document.

Jung, H.C., Getirana, A., Arsenault, K.R., Holmes, T.R., McNally, A., 2019. Uncertainties in evapotranspiration estimates over west Africa. Rem. Sens. 11, 892.
Kang, E.L., Cressie, N., Shi, T., 2010. Using temporal variability to improve spatial mapping with application to satellite data. Can. J. Stat. 38, 271–289.
Khan, M.S., Liaqat, U.W., Baik, J., Choi, M., 2018. Stand-alone uncertainty characterization of gleam, gldas and mod16 evapotranspiration products using an extended triple collocation approach. Agric. Forest Meteorol. 252, 256–268.
Kiptala, J.K., Mohamed, Y., Mul, M.L., Van der Zaag, P., 2013. Mapping evapotranspiration trends using Modis and Sebal model in a data scarce and heterogeneous landscape in eastern Africa. Water Resour. Res. 49, 8495–8510.
Li, M., Kang, E.L., Cawse-Nicholson, K., Braverman, A., 2019. Multivariate Spatial Modeling for Large Data with Remote Sensing Applications. Technical Report. University of Cincinnati.
Ma, P., Kang, E.L., 2019. Fused Gaussian process for very large spatial data. J. Comput. Graph. Stat. https://doi.org/10.1080/10618600.2019.1704293.
Ma, P., Kang, E., Braverman, A., Nguyen, H., 2019. Spatial statistical downscaling for constructing high-resolution nature runs in global observing system simulation experiments. Technometrics 61, 322–340.
Morton, C.G., Huntington, J.L., Pohll, G.M., Allen, R.G., McGwire, K.C., Bassett, S.D., 2013. Assessing calibration uncertainty and automation for estimating evapotranspiration from agricultural areas using metric. JAWRA J. Am. Water Resour. Assoc. 49, 549–562.
Mu, Q., Zhao, M., Running, S.W., 2011. Improvements to a modis global terrestrial evapotranspiration algorithm. Rem. Sens. Environ. 115, 1781–1800.
Myneni, R., Knyazikhin, Y., Park, T., NASA, M.S., 2015. MOD15A3H MODIS/Combined Terra + Aqua Leaf Area Index/FPAR Daily L4 Global 500m SIN Grid. Technical Report. NASA LP DAAC.
Nguyen, H., Cressie, N., Braverman, A., 2012. Spatial statistical data fusion for remote sensing applications. J. Am. Stat. Assoc. 107, 1004–1018.
Norman, J.M., Kustas, W.P., Humes, K.S., 1995. A two-source approach for estimating soil and vegetation energy fluxes from observations of directional radiometric surface temperature. Agric. Forest Meteorol. 77, 263–293.
Norman, J., Anderson, M., Kustas, W., French, A., Mecikalski, J., Torn, R., Diak, G., Schmugge, T., Tanner, B., 2003. Remote sensing of surface energy fluxes at 10^1-m pixel resolutions. Water Resour. Res. 39.
Saha, S., et al., 2011. NCEP Climate Forecast System Version 2 (CFSv2) Selected Hourly Time-Series Products, Technical Report. Research Data Archive at the National Center for Atmospheric Research, Computational and Information Systems Laboratory.
Shi, T., Cressie, N., 2007. Global statistical analysis of MISR aerosol data: a massive data product from NASA's Terra satellite. Environmetrics 18, 665–680.
Su, Z., 2002. The Surface Energy Balance System (SEBS) for estimation of turbulent heat fluxes. Hydrol. Earth Syst. Sci. 6, 85–99.
Survey, U.G., 2015. Landsat Surface Reflectance Data (Ver. 1.1, March 27, 2019): U.S. Geological Survey Fact Sheet 2015-3034. Technical Report.
Tzeng, S., Huang, H.-C., 2018. Resolution adaptive fixed rank kriging. Technometrics 60, 198–208.
USGS, 2004. Shuttle Radar Topography Mission, 1 Arc Second Scene SRTM_u03_n008e004, Unfilled Unfinished 2.0, Technical Report. Global Land Cover Facility, University of Maryland, College Park, MD February 2000.